Impact of pore size on the transport properties of nanoporous $LiNi_2O_4$ spinel

Donald Hlungwani*, *Raesibe Sylvia* Ledwaba and *Phuti* Ngoepe

Materials Modelling Centre, University of Limpopo, Private Bag x1106, Sovenga 0727, South Africa

Abstract. Nanostructuring of lithium-ion battery cathode materials is one of the most effective techniques for optimizing their electrochemical performance for large-scale applications such as electric vehicles. The partial substitution of Mn^{3+} with $Ni^{2+/3+}$ in $LiMn_2O_4$ spinel has shown improved rate-performance attributed to the increased Li^+ diffusion pathway due to the shortened M-O (M = Mn, Ni) average bond length, which sparked interest in the exploration of $LiNi_2O_4$ as a prospective cathode material for lithium-ion batteries (LIBs). In this study, the role of pore size on the transport properties of Li^+ in $LiNi_2O_4$ is explored since the practical capacity and rate performance of lithium ion battery cathode materials are affected by transport properties such as diffusion and conductivity. The diffusion coefficients of lithium ions in $LiNi_2O_4$ nanoporous structures with pore diameters of 1.1, 2.1, and 3.0 nm were found to be 7.99×10^{-13}, 3.03×10^{-12}, and 1.77×10^{-9} cm^2/s, respectively. Moreover, the ionic conductivity of lithium ions was also determined and found to be 1.25×10^{-8}, 4.28×10^{-8}, and 1.92×10^{-5} S/cm. Therefore, ionic conductivity and diffusion increase with increasing pore size. Furthermore, a large surface area was observed for the nanomaterial with a larger pore size. A larger surface area offers high contact between the electrolyte and the cathode material, which yields high practical capacities. As such, high-rate capabilities and improved cycle performance can be achieved by increasing the pore size to determine optimal pore diameters of nanoporous cathode materials.

1. Introduction

The search for affordable and high-energy dense cathode materials is ongoing and at the forefront in the research community for advancing the performance of lithium-ion batteries. Particularly for application in electric vehicles and the continued support of the exponentially growing market of portable electronics. To date, the positive electrode material remains the most expensive component of a lithium-ion battery (LIB) as compared to the anode and the electrolyte [1]. Moreover, the amount of energy that can be extracted from LIBs is determined by the cathode material since all the lithium ions that participate in the oxidation reduction during the discharge process are extracted from the cathode. $LiCoO_2$ has been the favourite choice for LIBs as a positive electrode material since their inception in 1970. They can provide acceptable discharge capacities at practical voltages (220 mAh/g) [2]. However, its

* Corresponding author: donald.hlungwani@gmail.com

© The Authors, published by EDP Sciences. This is an open access article distributed under the terms of the Creative Commons Attribution License 4.0 (https://creativecommons.org/licenses/by/4.0/).

application is limited in electric vehicles due to the high cost of cobalt and thermal instabilities. As a result, other $NaFeO_2$-type cathode materials have also been looked into. $LiMnO_2$ and $LiNiO_2$ also demonstrate high initial discharge capacities [3, 4]. However, they perform poorly during cycling due to irreversible structural changes. The active search for a next-generation cathode material also led to the exploration of Li_2MnO_3, which has a theoretical capacity of 458 mAh/g [5]. The presence of manganese in the materials sets it out as the most cost-effective option as compared to $LiCoO_3$. Nevertheless, its initial discharge requires an activation process, which results in the loss of oxygen. Lithium-manganese-oxide with a spinel structure ($LiMn_2O_4$) also evoked considerable research interest as a future cathode material for lithium-ion batteries. The material is environmentally benign, thermally stable, and inexpensive due to the abundance of manganese. Moreover, its structure offers three-dimensional channels, which facilitate high-rate capabilities that are crucial in applications such as electric vehicles. However, during cycling, the material suffers performance attenuation ascribed to the following: (a) the formation of Mn^{3+} and Mn^{4+} from Mn^{3+} through the disproportionation reaction ($2Mn^{3+} = Mn^{4+} + Mn^{2+}$), (b) the asymmetrical distribution of Li^+ in [Mn_2O_4], and (c) the lattice instabilities caused by the Jahn-Teller effect [6, 7]. However, the disproportionation reaction and the Jahn-Teller effects are the major causes of the performance decline during operation.

A significant number of studies concur on the reduction of the concentration of Mn^{3+} in the structure [8, 9, 10]. The replacement of Mn^{3+} with cations such as Al, Co, Ti, Cr, Mg, etc. is a way to reduce the Jahn-Teller active manganese ions and to strengthen the λ-Mn_2O_4 octahedron. Wang et al. employed the high-temperature solid-state approach to synthesise a Mg-doped $LiMn_2O_4$ spinel. The concentration of Mn^{3+} in the material was successfully lowered, and a capacity of ~92 mAh/g was observed after 500 discharge cycles of the initial capacity of 113 mAh/g [11]. Furthermore, Xu and colleagues improved the cycling stability of $LiMn_2O_4$ by replacing some of the manganese in the structure with Co [9]. Moreover, Liu and co-workers discovered that partially substituting Mn with Ni results in the oxidation of Mn^{3+} ions, which are adjacent to Ni^{2+}, into Mn^{4+}, thus increasing the average oxidation of manganese in the structure. This ameliorates the reported Jahn-Teller distortion and enhances cyclic performance [12]. However, the impact of cation-doping on the transport properties and nanostructuring of doped $LiMn_2O_4$ spinel materials has not been fully explored. Transport properties such as diffusion and ionic conductivity affect the amount and rate at which energy can be extracted from the material. Nanoarchitectured materials exhibit attractive properties such as high surface area, endurance to mechanical strain, and enhanced rate capabilities. Hence, in this study, the role of pore size on the transport properties of Li^+ in $LiNi_2O_4$ nanoporous is explored. This is a preliminary study for understanding the performance of pure $LiNi_2O_4$ nanoporous to guide the doping of $LiMn_2O_4$ spinel with Ni. $LiNi_2O_4$ nanoporous structures with varying pore sizes will be generated. Consequently, the impact of the pore size will be probed to guide the development of affordable, high-energy, and high-power dense lithium-ion batteries.

2. Method

Molecular dynamics (MD) simulations are utilized to investigate the microstructural properties of nanostructured $LiNi_2O_4$ spinel. The DLPOLY classical simulation code was chosen for carrying out the MD calculations [13]. Moreover, the simulated amorphization and recrystallization technique was employed to generate nanostructured $LiNi_2O_4$ materials, which are comparable to materials synthesized in experiments.

2.1 Potential model

All the calculations in this work are based on the Born model of ionic solids, which provides a way for evaluating the energy of a lattice. It gives an acceptable account of the contribution of electrostatics and short-range interactions. Henceforth, Coulomb's description of point charges and the Buckingham interatomic potential function were selected to capture these contributions (electrostatics and short-range interactions) to the total energy. Therefore, the long-range contribution to the total energy was calculated using equation 1.

$$U_{ij} = \frac{q_i q_j}{4\pi\varepsilon_0 r_{ij}} + Ae^{-Br} - \frac{\lambda}{r^6} \qquad (1)$$

The ionic charges of two interacting spheres are represented by q_i and q_j, where r is the interatomic separation. A and B are parameters of the repulsive part of the Buckingham potential function, and λ is the parameter of the attractive part of the function. Moreover, the A, B, and λ parameters for all the interactions considered in this work were derived elsewhere [14, 15, 16].

2.2 Generation of nanoporous $LiNi_2O_4$.

A $LiNi_2O_4$ supercell shown in figure 1 (a) was successfully optimized with the METADISE code and consecutively amorphized under the microcanonical ensemble [17]. The amorphized structure shown in figure 1(b) was then used to generate amorphous nanoporous $LiNi_2O_4$ structures with pore diameters of 1.1, 2.1, and 3.0 nm, as shown in figures 1(c), (d), and (e), respectively. The amorphous nanoporous $LiNi_2O_4$ materials were generated under the isothermal-isobaric ensemble. An isothermal-isobaric ensemble keeps the number of particles, temperature, and pressure of the system constant, which allows the variation of the volume of the system. This facilitates the generation of nanoporous structures. Subsequently, the amorphous nanoporous structures were then recrystallized using the canonical ensemble. The temperature of the system was scaled using the Nose-Hoover thermostat, and the structures were calibrated for 50 000 times in steps of 3 fs.

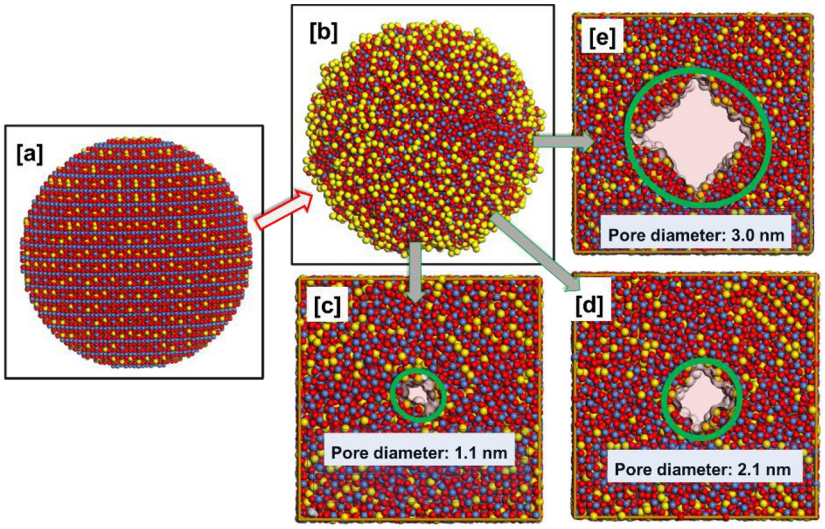

Fig. 1. (a) A crystalline $LiNi_2O_4$ nanosphere (LNO) was used to generate (b) an amorphous LNO nanosphere. Amorphous LNO nanoporous structures with pore diameters (c) 1.1, (d) 2.1, and (e) 3.0 nm were generated from the (b) amorphous LNO spinel nanosphere under the NPT ensemble.

3. Results and discussion

3.1 Potential X-ray diffraction (XRD) patterns

The nanoporous $LiNi_2O_4$ structures with pore diameters of 1.1, 2.1, and 3.0 nm were successfully generated with the simulated amorphization and recrystallization technique. The recrystallized structures were further cooled and characterized using XRD patterns. Figure 2 (a) shows the XRD pattern of the nanoporous material with a pore diameter of 1.1 nm. The XRD peaks are well resolved, which evidences successful recrystallization of the 1.1 nm structure. All the major spinel XRD peaks {(111), (311), (222), (400), (331), (511), (440), and (531)} can be clearly observed from the XRD graph. The XRD pattern compares well to the XRD pattern calculated by Thomas et al [18]. Furthermore, XRD peaks associated with the Ni_3O_4 impurity phase are also observed at $2\theta = \sim 30°$, while small XRD peaks ascribed to the Li_2MnO_3 impurity phase are observed after the (331), and (531) reflections. Figure 2 (b) depicts the XRD plot of the nanoporous $LiNi_2O_4$ structure with a pore diameter of 2.1 nm. All the $LiNi_2O_4$ spinel characteristic peaks are well resolved, which shows the successful recrystallization of the material. The XRD pattern can be indexed to a cubic spinel structure of space Fd-3m symmetry. The Ni_3O_4 and Li_3MnO_3 high-temperature impurity phases are also noted in this material. However, the XRD patterns associated with these phases are small, which indicates that they are in small concentrations in the material. Moreover, the XRD pattern compares well to the XRD pattern of $LiNi_2O_4$ calculated by Thomas et al [18]. Figure 2 (c) illustrates the XRD pattern of the nanoporous $LiNi_2O_4$ polymorph with a pore diameter of 3.0 nm. Diffraction is observed in the (111), (311), (222), (400), (331), (511), (440), and (531) planes and can be indexed to a spinel lattice with Fd-3m cubic symmetry. The diffraction peaks are also observed in the XRD pattern calculated in experiment shown in figure 2(d). Moreover, small impurity peaks of the Ni_3O_4 and Li_2MnO_3 phases are also noted in the XRD patterns and are confirmed by the XRD peaks in figures 2 (e) and (f).

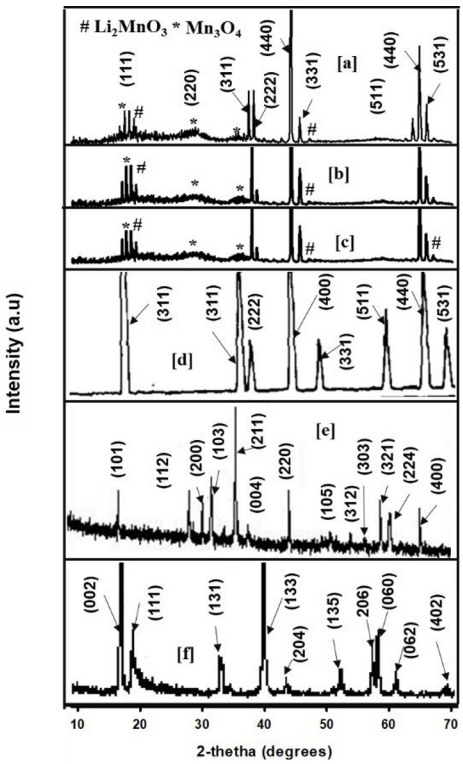

Fig. 2. (a) XRD patterns of nanoporous $LiNi_2O_4$ with pore diameters of (a) 1.1, (b) 2.1, and (c) 3.0 nm compared to the XRD patterns of (d) $LiNi_2O_4$ [18], (e) Mn_3O_4 [19], and (f) Li_2MnO_3 [20].

3.2 Impact of pore diameter on the volume and surface area of nanoporous $LiNi_2O_4$

Figure 3 (a) illustrates the role of pore size on the volume of the nanoporous $LiNi_2O_4$ structures with pore diameters of 1.1, 2.1, and 3.0 nm. The 1.1, 2.1, and 3.0 nm nanoporous materials were generated in simulation cells of dimensions 67 x 67 x 67 $Å^3$, 69 x 69 x 69 $Å^3$, and 75 x 75 x 75 $Å^3$, respectively. Therefore, the 3.0 nm $LiNi_2O_4$ nanoporous structure has the largest volume. Furthermore, the 1.1 nm $LiNi_2O_4$ nanoporous material has the smallest volume compared to the 2.1 and 3.0 nm nanoarchiectures. A larger volume facilitates the generation of a large pore size. Moreover, the large volume provides extra room for atoms to settle, which in turn offers clear diffusion channels. This is positive for high-rate capabilities, which are crucial for large-scale applications such as electric vehicles. Furthermore, the surface area of these nanoporous polymorphs was also examined, as illustrated in figure 3(b). The surface areas of 12047.7, 15504.17, and 22158.57 $Å^2$ were noted for the 1.1, 2.1, and 3.0 nm nanoporous structures, respectively. Therefore, the structure generated in a bigger simulation cell (75 x 75 x 75 $Å^3$) possesses the highest surface area (22158.57 $Å^2$). As such, increasing the pore size also increases the surface area of the nanomaterial. The surface area is proportional to the number of active redox sites and the contact between the electrolyte and the cathode material. As such, a higher surface area will result in improved rate capabilities.

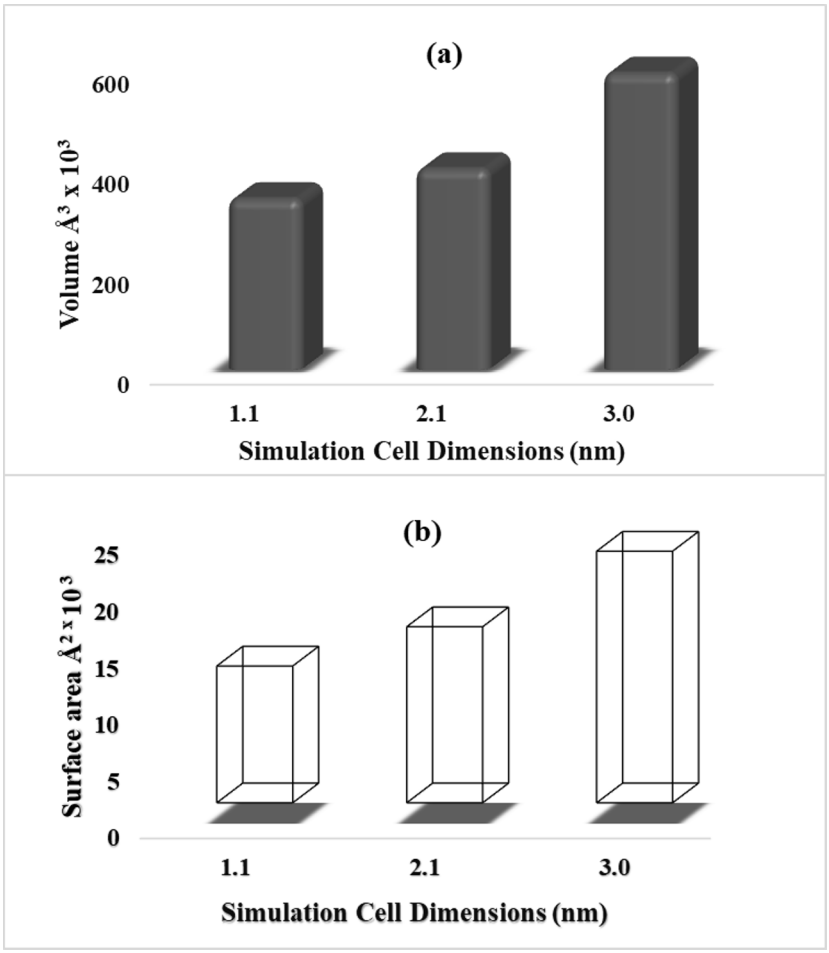

Fig. 3. Illustration of the (a) volume of the $LiNi_2O_4$ nanoporous materials with pore diameters of 1.1, 2.1, and 3.0 nm. (b) The calculated surface area of the nanoporous materials as a function of pore diameter.

3.3 Li^+ Transport properties of nanoporous $LiNi_2O_4$

The diffusion of particles can be related to mean squared displacement (MSD) using the following equation:

$$< \boldsymbol{r}_i^2 > = 6D_t + C \qquad (2)$$

where $< \boldsymbol{r}_i^2 >$ denotes the MSD, D_t captures the rate of diffusion, t is the time, and C is a constant. The movement of Li^+ ions in the $LiNi_2O_4$ nanoarchitectures with pore diameters of 1.1, 2.1, and 3.0 nm is examined with the MSD plots shown in figure 4 (a). The mean square of the displacement of a particle that imitates a random walk is proportional to the time elapsed. Therefore, the overall mobility of particles can be inferred from a MSD plot, which gives insights into their diffusivity. The definition of the mean square displacement over time t is given by equation 1, where r is the position of the particle.

$$< \boldsymbol{r}_i^2 > = \frac{1}{3} < |\boldsymbol{r}_i\,(t) - \boldsymbol{r}_i\,(0)|^2 > \qquad (3)$$

The MSD plot of the 1.1 nanostructure is plateauing when compared to the MSD plot of the 2.1 nanostructure, which can be clearly seen from the insert figure (figure 4(b)). This shows that lithium ions have higher mobility in the 2.1 nanostructure than in the 1.1 nanostructure. Furthermore, the movement of lithium ions in the 1.1 and 2.1 nanoporous materials does not transcend distances of 0.7 and 1.3 Å in 1400 ps, respectively. The mobility of lithium ions in the nanoporous structure with a pore diameter of 3.0 nm increases with time, as shown by the graph in figure 4. In 1400 ps, lithium ions cover distances of ~35 Å in the 3.0 nm nanomaterial. Therefore, the mobility of lithium ions increases with increasing pore diameter.

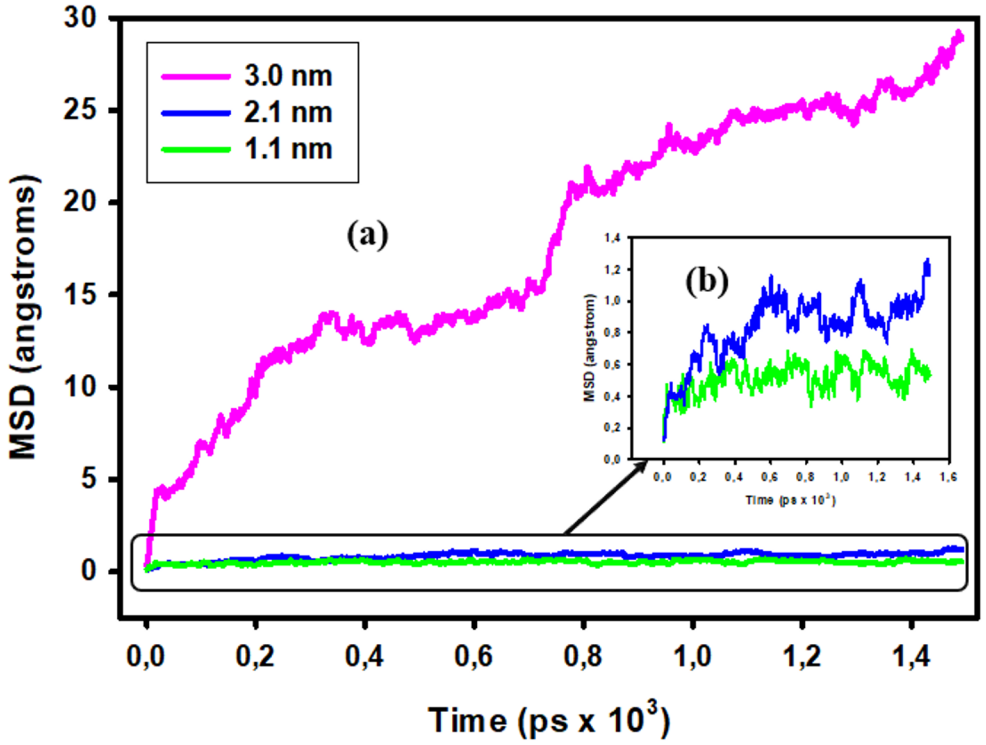

Fig. 4. Comparison Mean Squared Displacement of Li^+ in $LiNi_2O_4$ particles with a pore diameter of (a) 1.1, 2.1, and 3.0 nm at a temperature of 300 K for distances between 0-1.2 Å and 0-30 Å.

The rate of diffusion is directly proportional to the slope of a MSD versus temperature graph. The diffusion of Li^+ was also investigated through the diffusion coefficients shown in figure 5. Figure 5 (a) shows the diffusion coefficients of the $LiNi_2O_4$ nanoporous structures with pore diameters of 1.1, 2.1, and 3.0 nm. The diffusion coefficients of lithium ions at 300 K in the 1.1 and 2.1 nm nanoporous materials are 7.99 x 10^{-13} and 3.03 x 10^{-12} cm^2/s, respectively. Furthermore, between temperatures of 200 K and 450 K, the diffusion coefficients of the 2.1 nm nanoporous structure are higher than the diffusion coefficients of the 1.1 nm structure. At 300 K, the diffusion coefficient of Li^+ in the 3.0 nm nanostructure is 1.77 x 10^{-9} cm^2/s. Therefore, lithium ions have higher diffusivity in the 3.0 nm nanostructure than in the 1.1 and 2.1 nm nanostructures. Additionally, in temperatures between 200 K and 450 K, the diffusion coefficients of Li^+ in the 3.0 structure are increasing linearly with increasing temperature. The conductivity of Li^+ in the. $LiNi_2O_4$ nanoporous structures was also investigated and calculated using the following equation:

$$\sigma = \frac{DC_f e^2}{K_b T} \qquad (4)$$

where D is the diffusion coefficient, C_f is the concentration of Li^+, and e is the charge of the lithium ion. Moreover, T is the temperature of the system, and K_b is the Boltzmann constant. Figure 6 captures the impact of pore size on the ionic conductivity of nanoporous $LiNi_2O_4$ structures (1.1, 2.1, and 3.0). At 300 K, the ionic conductivities of Li^+ in the 1.1 nm and 2.1 nm structures are 1.25 x 10^{-8} and 4.28 x 10^{-8} S/cm, respectively. The conductivity of Li^+ in the 2.1 nm structure is higher than in the 1.0 nm structure at temperatures between 200 K and 450 K, as illustrated in figure 6 (a). The ionic conductivity of lithium is 1.92 x 10^{-5} S/cm in the $LiNi_2O_4$ nanoporous structure with a pore diameter of 3.0 nm, which is higher than in the 1.1 and 2.1 nm nanoporous structures. Higher Li^+ diffusion and ionic conductivity will result in enhanced rate capabilities and will also boost the retrieval of lithium ions in the structure, which will improve the practical capacity of the material.

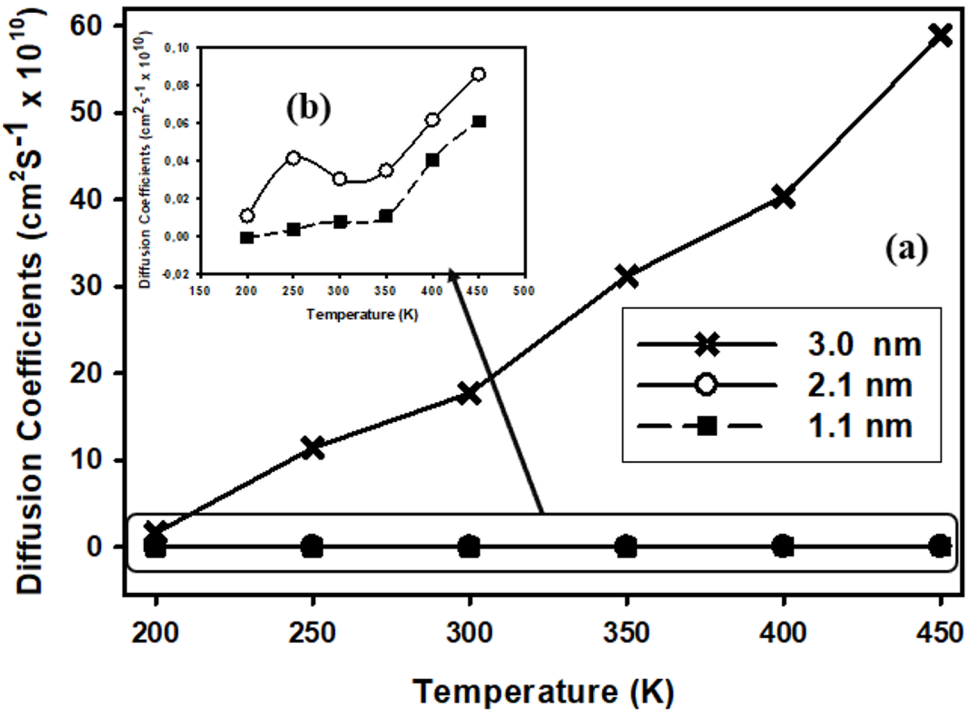

Fig. 5. (a) The rate of Li^+ diffusion in $LiNi_2O_4$ nanoporous with pore diameters of 1.1, 2.1, and 3.0 nm. (b) The insert of the rate of Li^+ diffusion in $LiNi_2O_4$ nanoporous with a pore diameter of 1.1 and 2.1 nm.

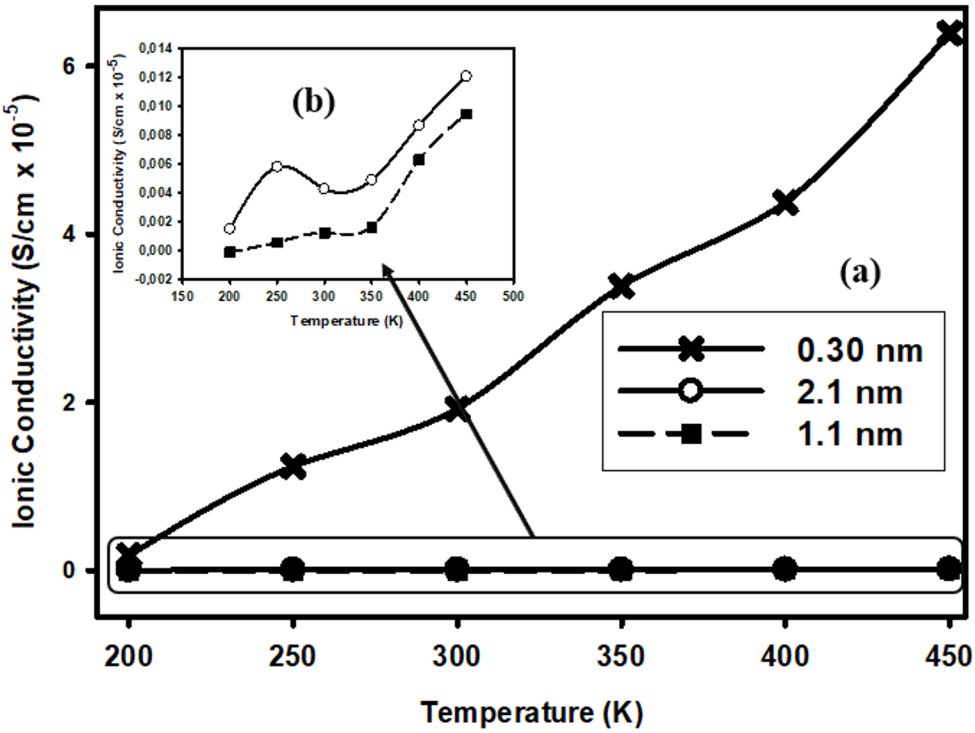

Fig. 6. Illustration of the Li^+ ionic conductivity in $LiNi_2O_4$ nanoporous materials with pore diameters of (a) 1.1, 2.1, and 3.0 nm. The insert of the ionic conductivity of Li^+ in a $LiNi_2O_4$ nanoporous structure with a pore diameter of 1.1 and 2.1 nm.

4. Conclusion

The impact of pore size on the transport properties of lithium ions in nanoporous $LiNi_2O_4$ structures was successfully investigated. The nanoporous structure with a bigger pore size was found to have a higher surface area. As such, the number of active redox sites and the contact between the cathode material and the electrolyte can be increased by increasing the pore size. Moreover, the mobility of lithium ions in $LiNi_2O_4$ nanoporous was found to increase with an increase in pore size. Furthermore, the nanoporous structure with a larger pore diameter was found to have the highest diffusion and ionic conductivity of Li^+. As such, the rate-capabilities of a nanoporous cathode material can be improved by increasing the pore size, which will also improve its practical capacity. Therefore, nanoarchitectured cathode materials can offer improved electrochemical performance in lithium-ion batteries and speed their utilization in EVs.

The authors acknowledge the Centre for High Performance Computing (CHPC) for computing resources and the National Research Foundation (NRF) for funding, grant number 133744.

References

[1] Li. Qi, Y. Wang, L. Kong, M. Yi, J. Song, D. Hao, X. Zhou, Z. Zhang, J. Yan, J. Energy Storage **67**, 107533-107533 (2023)

[2] Y. Lyu, X. Wu, K. Wang, Z. Feng, T. Cheng, Y. Liu, M. Wang, R. Chen, L. Xu, J. Zhou, Y. Lu, Adv. Energy Mater **11**, 2000982-2000982 (2021)

[3] X Zhu, F. Meng, Q. Zhang, L. Xue, H. Zhu, S. Lan, Q. Liu, J. Zhao, Y. Zhuang, Q. Guo, B. Liu, Nat. Sustain **4**, 392-401 (2021)

[4] F. Riewald, P. Kurzhals, M. Bianchini, H. Sommer, J. Janek, H.A. Gasteiger, J. Electrochem. Soc **169**, 20529-20529 (2022)

[5] Z. Chen, W. Zhang, J. Liu, M. Zhang, S. Li, F. Pan, Adv. Mater **1**, 2403307-2403307 (2024)

[6] X. Hou, X. Liu, H. Wang, X. Zhang, J. Zhou, M. Wang, Energy Storage Mater **57**, 577-606 (2023)

[7] Q. Yu, P. Li, Q. Guo, IJPAC **25**, 14-21 (2024)

[8] S. Ren-ji, Z. Tong, Z. Yu, X. Xin-yan, W. Tao, M. Zi-yang, T. Pei-yuan, H. Xiang-ping, J. Jian-bing, Solid State Ion **404**, 116434-116434 (2024)

[9] W. Xu, S. Guo, Q. Li, S. Xia, F. Cheng, F. Sui, R. Qi, Y. Ca, R. Huang, Vacuum **219**, 112724-112724 (2024)

[10] L. Huang, Y. Wu, Ceram. Int **50**, 5150-5159 (2024)

[11] Y. Wang, S. Luo, P. Li, H. Zhang, S. Yan, H. Li, Y. Tian, F. Teng, Q. Wang, A. He, F. Zhuge, Mater. Today Commun **33**, 104391-104391 (2022)

[12] W. Liu, H. Xu, Q. Zhou, Y. Dai, W. Hu, H. Li, Journal of Electronic Materials **49**, 5523-5527 (2020)

[13] W. Smith, T.R. Forester, J. Mol. Graph **14**, 136-141 (1996)

[14] R.R. Maphanga, D.C. Sayle, T.X. Sayle, P.E. Ngoepe, Phys. Chem. Chem. Phys **13**, 1307-1313 (2011)

[15] T.X. Sayle, C.R.A. Catlow, R.R. Maphanga, P.E. Ngoepe, D.C. Sayle, J. Am. Chem **127**, 12828-12837 (2005)

[16] D. Hlungwani, P.E. Ngoepe, R.S. Ledwaba, SAIP Proceedings **1**, 157-163 (2023)

[17] W.G. Watson, E.T. Kelsey, N.H. de Leeuw, D.J. Harris, J. Chem. SOC., Faraday Trans **92**, 433-438 (1996)

[18] M.G.S.R. Thomas, W.I.F. David, J.B. Goodenough, P. Groves, Mater. Res. Bull **20**, 1137-1146 (1985)

[19] Z. Wu, K. Yu, Y. Huang, C. Pan, Y. Xie, Chem. Cent. J **1**, 1-9 (2007)

[20] S. Li, D. Lei, AIP Conf. Proc **1**, 1-1 (2017)